Nanoscale

PAPER

View Article Online
View Journal | View Issue

Cite this: *Nanoscale*, 2025, **17**, 12465

Rubidium intercalation in epitaxial monolayer graphene†

Letizia Ferbel, *[a] Stefano Veronesi, [a] Tevfik Onur Mentes,[b] Lars Buß,[c] Antonio Rossi,[d] Neeraj Mishra,[d] Camilla Coletti, [d] Jan Ingo Flege, [c] Andrea Locatelli[b] and Stefan Heun [a]

Received 28th January 2025,
Accepted 15th April 2025

DOI: 10.1039/d5nr00417a

rsc.li/nanoscale

Alkali metal intercalation of graphene layers has been of particular interest due to potential applications in electronics, energy storage, and catalysis. Rubidium (Rb) is one of the largest alkali metals and among the least investigated as an intercalant. Here, we report a systematic investigation, with a multi-technique approach, of the phase formation of Rb under epitaxial monolayer graphene on SiC(0001). We explore a wide phase space with two control parameters: the Rb density (*i.e.*, deposition time) and sample temperature (*i.e.*, room and low temperature). We reveal the emergence of (2 × 2) and $(\sqrt{3} \times \sqrt{3})$ R30° structures formed by a single alkali metal layer intercalated between monolayer graphene and the interfacial C-rich reconstructed surface, also known as the buffer layer. Rb intercalation also results in strong n-type doping of the graphene layer. Upon progressively annealing to higher temperatures, we first reveal the diffusion of Rb atoms, which results in the enlargement of intercalated areas. As desorption sets in, intercalated regions progressively shrink and fragment. Eventually, at approximately 600 °C, the initial surface is retrieved, indicating the reversibility of the intercalation process.

1 Introduction

Alkali metals (AMs) are relevant in many fields due to their low electronegativity, high reactivity, and catalytic properties. Research on AM intercalation between graphene layers started in the early 1920s with graphite intercalation compounds (GICs).[1] The insertion of AMs between graphene layers presents promising opportunities for use in electronics, energy storage, and catalysis.[2–4] However, understanding the details of AM intercalation at specific graphene interfaces remains a priority.

Lithium (Li), sodium (Na), and potassium (K) have been widely studied for their application in rechargeable ion batteries and electrical conductors.[3,5] Intercalation of potassium in graphene has also sparked interest due to its superconductivity at relatively high temperatures[6] and the extended van Hove singularities in the graphene band structure around the M point,[7] while cesium (Cs) intercalated layers have been demonstrated to realize a two-dimensional Fermi gas.[8] Interestingly, Rb-intercalated bilayer graphene has been shown to exhibit a metallic interlayer state,[9–11] which is associated with superconductivity in intercalated graphene compounds.[12,13] Furthermore, intercalated rubidium (Rb) has come under focus in the advancing field of ultracold-atom dispensers.[14] Rb also appears to be very promising and worth investigating in the field of energy storage.[15]

A clear understanding of the atomic arrangement of AM atoms between graphene layers is crucial for optimizing such graphene-based devices, as this influences the electronic structure and thus the final properties of the material. Highly ordered structures of AM intercalants have been reported to appear in carbon-layered structures ranging from bilayer graphene to bulk graphite. In these systems, K, Rb, and Cs atoms form a (2 × 2) superstructure with respect to the graphene lattice[5,9,16–19] (sketched in Fig. 1(a)), while the intercalation of Li leads to a more densely packed superstructure of $(\sqrt{3} \times \sqrt{3})$ R30° periodicity with respect to the graphene lattice[5,20] (sketched in Fig. 1(b)). However, the ordered Rb intercalation of graphene monolayers has not yet been reported. So far, only the formation of an ordered Rb (2 × 2) overlayer on quasi-free-standing monolayer graphene on SiC(0001) has been reported.[21]

Here we reveal, with microscopic detail, the processes of intercalation and de-intercalation of Rb underneath monolayer graphene on SiC(0001). We study the Rb intercalation morphologies and de-intercalation dynamics by using *in situ* con-

[a]*NEST, Istituto Nanoscienze-CNR and Scuola Normale Superiore, Piazza S. Silvestro 12, 56127 Pisa, Italy. E-mail: letizia.ferbel@sns.it; Tel: +39 050 509882*
[b]*Applied Physics and Semiconductor Spectroscopy, Brandenburg University of Technology Cottbus-Senftenberg, 03046 Cottbus, Germany*
[c]*Elettra-Sincrotrone Trieste S.C.p.A., Strada Statale 14, km 163.5, I-34149 Basovizza, Trieste, Italy*
[d]*Center for Nanotechnology Innovation@NEST, Istituto Italiano di Tecnologia, Piazza S. Silvestro 12, 56127 Pisa, Italy*

† Electronic supplementary information (ESI) available. See DOI: https://doi.org/10.1039/d5nr00417a

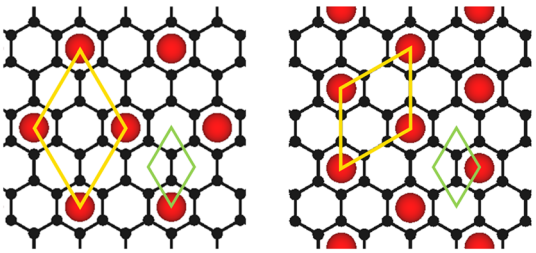

Fig. 1 Schematic top-view representation of the AM distribution: (a) in the (2 × 2) superstructure and (b) in the $(\sqrt{3} \times \sqrt{3})$ R30° superstructure. Black circles represent C atoms, while red circles represent AM atoms. The graphene unit cell is highlighted by a green rhombus, while the unit cells of the superstructures are highlighted in yellow.

ventional and micro-spot low-energy electron diffraction (LEED and μ-LEED), scanning tunneling microscopy (STM), and low-energy electron microscopy (LEEM) in conjunction with density functional theory (DFT). Our results shed light on the Rb intercalation mechanism below graphene and demonstrate that 2D ordering of intercalated Rb atoms can be achieved even in monolayer graphene.

2 Experimental

Graphene was epitaxially grown on nominally on-axis n-type 6H-SiC(0001) wafers. The graphene growth was performed in a BM-Aixtron reactor *via* silicon sublimation at temperatures of 1250–1300 °C under an argon atmosphere.[22,23] Here, we use surfaces consisting of a mixture of buffer-layer and monolayer graphene regions. The graphene quality, uniformity, and composition were first assessed in air by atomic force microscopy and Raman spectroscopy. Once in the ultra-high vacuum chamber (UHV, base pressure $<1 \times 10^{-10}$ mbar), the as-grown graphene samples were degassed at 600 °C to eliminate adsorbates. Subsequently, the graphene quality was further verified in UHV *via* LEED and STM, and in some cases, also by LEEM.

Rb was evaporated using a commercial dispenser (SAES Getters Inc.) onto the graphene surface held either at room temperature (RT) or at low temperature (LT, 100–140 K). The Rb deposition time accounts for the time the sample is directly facing the Rb evaporator after reaching the desired deposition conditions (the evaporator current and flux were kept constant during deposition). Due to the different geometry of the evaporator set-up, the Rb yield in the LEEM experiment was ~60 times lower than the Rb yield in the STM experiment. Rb diffusion and de-intercalation were achieved by annealing the samples for 10 min at temperatures in the range of 50–800 °C in the case of RT-Rb deposition and in the range of 160–300 K in the case of LT-Rb deposition.

STM data were acquired with a VT-RHK-STM operating in constant current mode, at RT, and under UHV conditions. STM images were processed with the Gwyddion software package.[24] The STM preparation chamber was equipped with a commercial LEED OCI BDL-600IR (spot size ~500 μm).

LEEM (resolution ~10 nm) and μ-LEED (spot size ~1 μm) measurements were performed using a SPELEEM III (Elmitec GmbH) setup at the Nanospectroscopy beamline (Elettra, Trieste).[25,26]

DFT calculations were performed using the projector augmented wave method as implemented in GPAW[27] using the Perdew–Burke–Ernzerhof (PBE)[28] parameterization of the generalized gradient approximation (GGA). Dispersion corrections were included using the Grimme D4 model (DFT-D4).[29–31] A 7 × 7 × 1 Monkhorst–Pack grid was used for integration of the 3D Brillouin zone and a cut-off energy of 400 eV was used for the plane wave basis set. A detailed discussion of the calculations is available in the ESI.†

3 Results

Fig. 2 shows the coverage-dependent evolution of the graphene LEED pattern as obtained after Rb deposition at room temp-

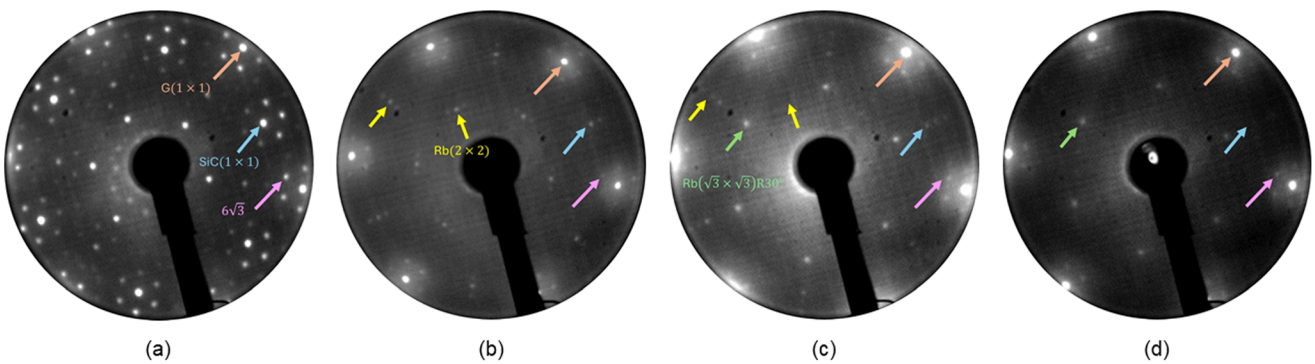

Fig. 2 Evolution of the LEED pattern upon Rb deposition on epitaxial graphene on SiC(0001) at room temperature. LEED patterns obtained from (a) the pristine graphene sample and after depositing Rb for (b) 1 min, (c) 2 min, and (d) 3 min. The graphene, SiC, and $6\sqrt{3}$ structures are indicated by peach, blue, and pink arrows, respectively. The Rb (2 × 2) and Rb $(\sqrt{3} \times \sqrt{3})$ R30° structures are highlighted by yellow and green arrows, respectively. Beam energy: (a) 60 eV, (b) 75 eV, (c) 60 eV, and (d) 65 eV.

erature. The diffraction pattern of the pristine sample (shown in Fig. 2(a)) shows the (1 × 1) graphene and (1 × 1) SiC substrate patterns as well as the characteristic $(6\sqrt{3} \times 6\sqrt{3})$ R30° moiré reconstruction (that will be referred to as $6\sqrt{3}$ in the following) originating from the interaction and partial bonding of the buffer layer with the SiC substrate.[32] After Rb deposition (Fig. 2(b)–(d)), the diffraction spots of the pristine sample change their relative intensities. The SiC and $6\sqrt{3}$ diffraction intensities weaken, but these spots do not disappear. On the other hand, the intensity of the graphene spots does not change and remains the brightest, suggesting the presence of Rb atoms below the graphene layer rather than being adsorbed. The presence of the $6\sqrt{3}$ pattern excludes the presence of Rb below the buffer layer. Consequently, these data suggest the presence of an Rb interlayer between the buffer layer and graphene, which attenuates the diffraction intensity of the layers below it. After Rb deposition for 1 min (shown in Fig. 2(b)), in the LEED pattern, an additional set of diffraction spots appears. These correspond to an ordered Rb superstructure with (2 × 2) periodicity with respect to graphene. With further Rb deposition (2 min, shown in Fig. 2(c)), a second set of additional diffraction spots develops. These are rotated by 30° compared to the graphene lattice and identified as a $(\sqrt{3} \times \sqrt{3})$ R30° superstructure, corresponding to an ordered Rb structure with higher density. The diffraction patterns of these two Rb-ordered superstructures coexist up to a saturation coverage, above which only the $(\sqrt{3} \times \sqrt{3})$ R30° structure remains (shown in Fig. 2(d)). These changes in the diffraction pattern indicate the formation of a well-ordered alkali metal layer sandwiched between the buffer layer and monolayer graphene whose structure evolves from a (2 × 2) to a $(\sqrt{3} \times \sqrt{3})$ R30° with increasing Rb coverage at RT.

At RT, the (2 × 2) superstructure is not stable. After about 20 min from the Rb deposition, all features in the LEED pattern originating from the (2 × 2) structure disappear completely. On the other hand, the denser $(\sqrt{3} \times \sqrt{3})$ R30° superstructure remains stable for at least several months under UHV conditions at RT.

Low-temperature Rb deposition followed by annealing cycles up to room temperature also results in a continuous evolution of the Rb interlayer from a (2 × 2) superstructure to a $(\sqrt{3} \times \sqrt{3})$ R30° superstructure (as reported by the diffraction analysis shown in Fig. S1 and S2 of the ESI†). By depositing Rb at 100–140 K, a low-intensity and diffuse (2 × 2) pattern develops. By progressively heating the sample, the (2 × 2) reflections get sharper while the diffuse background decreases, indicating increased ordering of the intercalated phase. At 190 K, the $(\sqrt{3} \times \sqrt{3})$ R30° pattern appears, coexisting with the (2 × 2) reconstruction. The (2 × 2) superstructure vanishes close to RT, while the $(\sqrt{3} \times \sqrt{3})$ R30° superstructure is visible in a wide temperature range above 190 K, including room temperature. This evolution of the LEED pattern suggests that initially a large amount of deposited Rb is adsorbed on the surface in a disordered manner. Diffusion is induced by annealing, which allows the phase transition between the (2 × 2) and $(\sqrt{3} \times \sqrt{3})$ R30° superstructures.

Further information is obtained from STM imaging. A few key modifications of the graphene surface due to Rb deposition can be identified. Fig. 3 reports the typical large-scale surface morphology obtained after Rb deposition at RT. As shown in Fig. 3(a), the step-terrace morphology of the pristine graphene/SiC sample can still be easily recognized, in addition to a wrinkle network that appears all over the monolayer graphene surface, but that avoids buffer layer regions. Wrinkles extend for several μm in length and have a height of a few nm and a width of tens of nm (as shown in the inset of Fig. 3(a)). They do not follow random directions, but mainly the 6-fold symmetry of graphene. Wrinkles in the uppermost graphene sheet are common for epitaxial graphene, yet they may never appear without intercalation.[33–36] In the present case, however, wrinkles were not observed on the surface prior to Rb evaporation, but readily appeared after Rb evaporation. Thus, here, the wrinkles observed are due to Rb atoms, which are likely intercalated below the sample surface and sit between the graphene and the buffer layer (since wrinkles avoid the buffer layer). In addition to the wrinkles, quite flat areas appear, shown and labeled as RbG in Fig. 3(b). These areas are Rb-intercalated graphene regions, which prevalently extend from the wrinkles and protrude ~325 pm above the monolayer graphene (as shown in the inset of Fig. 3(b)). On the buffer layer, we only found randomly distributed Rb atoms adsorbed on the surface with no indication pointing towards intercalation. Low-temperature Rb deposition results in the same sample morphology, with the additional presence of an extensive disordered Rb adlayer on the monolayer graphene regions.

RbG areas often show the morphology reported in Fig. 4. These topographies show the presence of a weak long-range $6\sqrt{3}$ modulation, also visible in the fast Fourier transform (FFT) of the STM image (inset of Fig. 4(a)), which evidences that the bonds between the SiC substrate and the buffer layer are still intact. As indicated in Fig. 4(b) and in Fig. S3(a) of the

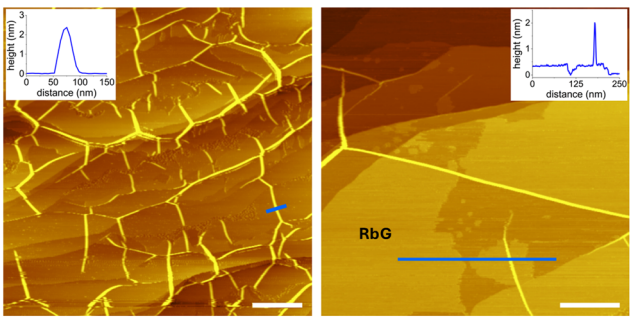

Fig. 3 (a) Overview STM scan of the graphene surface obtained after Rb deposition for 3 min at RT showing a wrinkle network. Inset of (a): cross-section taken across a wrinkle, along the blue line in (a). (b) Close-up view of monolayer graphene showing the wrinkle network and Rb-intercalated regions, labeled as RbG. Inset of (b): cross-section taken across RbG regions, along the blue line in (b). Scale bar: (a) 500 nm and (b) 100 nm. Scan parameters [*V*, *I*]: (a) [2 V, 100 pA] and (b) [–1 V, –100 pA].

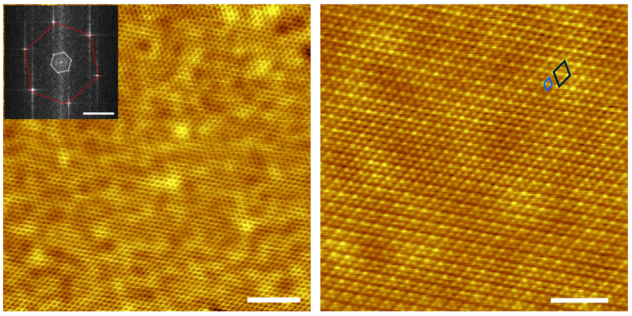

Fig. 4 STM topographic images of Rb-intercalated regions in monolayer graphene showing Rb (2 × 2) ordering. (a) STM scan showing the $6\sqrt{3}$ -moiré reconstruction and the Rb (2 × 2) ordering highlighted in the corresponding FFT shown in the inset by white and red hexagons, respectively. (b) Atomically resolved STM scan showing the Rb (2 × 2) arrangement together with the graphene lattice, highlighted by black and blue rhombi, respectively. Scale bar: (a) 5 nm and inset of (a) 2 nm^{-1}, and (b) 2 nm. Scan parameters [*V*, *I*]: (a) [500 mV, 300 pA] and (b) [−300 mV, −100 pA].

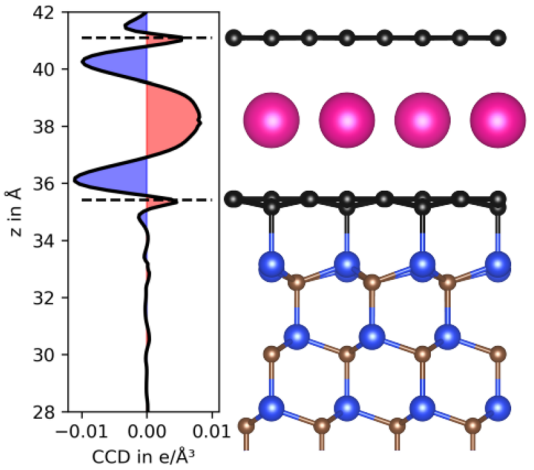

Fig. 5 Charge density difference (CDD) and optimized geometry of the Rb-intercalated (2 × 2) structure in monolayer graphene on SiC(0001) obtained from DFT analysis. Due to Rb intercalation, the graphene-buffer layer separation increases to 5.77 Å, which is in good agreement with the results obtained by STM for the Rb-(2 × 2) reconstruction.

ESI,† the graphene lattice is resolved all over the investigated area, suggesting that Rb atoms do not reside on the surface but rather below the topmost graphene layer, consistent with the strong graphene diffraction spots seen in Fig. 2. A larger hexagonal pattern showing a peak-to-peak distance of 492 pm can be resolved as well. This is consistent with a (2 × 2) ordering with respect to the graphene lattice. The local variation in height is at most 30 pm, which is much smaller than the ionic radius of Rb atoms (152 pm),[37] again compatible with an Rb-intercalated phase. The (2 × 2) RbG regions have an apparent height difference relative to the non-intercalated monolayer graphene of (301 ± 68) pm, which is in good agreement with the layer separation obtained by DFT for a single (2 × 2)-Rb interlayer (as reported in Fig. 5 and in section S5 of the ESI†). Thus, the (2 × 2) structure is formed by a single Rb interlayer sandwiched between monolayer graphene and the buffer layer.

Other RbG regions reveal the morphology shown in Fig. 6. Again, these topographies show the presence of a weak long-range $6\sqrt{3}$ reconstruction, also visible in the FFT of the STM image (inset of Fig. 6(a)). As seen in Fig. 6(b) and in Fig. S4(a) of the ESI,† the graphene lattice is observed all over the surface, and a larger hexagonal pattern showing a peak-to-peak distance of 426 pm and a unit cell rotated by 30° with respect to the graphene is observed as well. This structure is consistent with Rb intercalated under the topmost graphene surface with a $(\sqrt{3} \times \sqrt{3})$ R30° ordering with respect to the graphene lattice. The $(\sqrt{3} \times \sqrt{3})$ R30° RbG regions have an apparent height difference measured with respect to the non-intercalated monolayer graphene of (354 ± 43) pm, a value that is again compatible with only a single alkali-metal intercalated layer. The slightly higher vertical spacing measured for $(\sqrt{3} \times \sqrt{3})$ R30°, compared to the (2 × 2) morphology, might be a result of differences in lateral compression between the two structures. The distance between Rb atoms in the (2 × 2) structure (492 pm) is close to that of Rb in the bulk (484 pm).[38] In the case of $(\sqrt{3} \times \sqrt{3})$ R30°, the distance between Rb atoms is 426 pm, and thus the lattice is laterally compressed by ~10% with respect to the bulk form. This would in turn increase the vertical spacing, thereby increasing the distance between the buffer layer and monolayer graphene. Therefore, the $(\sqrt{3} \times \sqrt{3})$ R30° superstructure is due to a single Rb interlayer sandwiched between the monolayer graphene and the buffer layer.

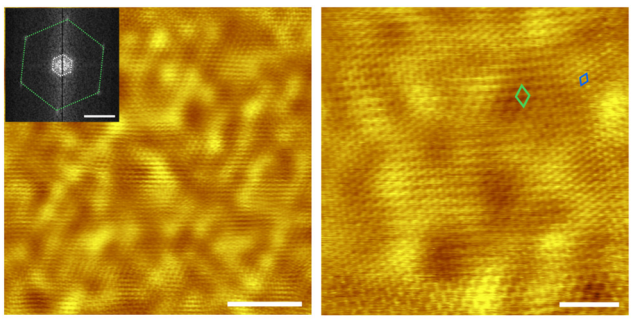

Fig. 6 STM topographic images of Rb-intercalated regions in monolayer graphene showing Rb $(\sqrt{3} \times \sqrt{3})$ R30° ordering. (a) STM scan showing the $6\sqrt{3}$ -moiré reconstruction and the Rb $(\sqrt{3} \times \sqrt{3})$ R30° ordering highlighted in the corresponding FFT shown in the inset by white and green hexagons, respectively. (b) Atomically resolved STM scan showing the Rb $(\sqrt{3} \times \sqrt{3})$ R30° arrangement together with the graphene lattice, highlighted by green and blue rhombi, respectively. Scale bar: (a) 5 nm and inset of (a) 2 nm^{-1}, and (b) 2 nm. Scan parameters [*V*, *I*]: (a) [100 mV, 90 pA] and (b) [90 mV, 90 pA].

Fully in agreement with the LEED characterization, both (2 × 2) and $(\sqrt{3} \times \sqrt{3})$ R30° Rb-ordered superstructures are resolved by STM. These correspond to a single ordered 2D alkali-metal interlayer arranged below the topmost graphene surface.

Additional insight comes from LEEM analysis, reported in Fig. 7 and in section S3 of the ESI.† LEEM is a well-suited technique for the investigation of intercalation processes. The energy-dependent coupling of the incoming electrons to the graphene interlayer states leads to a characteristic modulation of the reflectivity, where the number of dips in the intensity–voltage (LEEM-IV) spectrum corresponds to the number of freestanding graphene layers.[39] Therefore, in strongly bound graphene systems, successful intercalation and decoupling of the graphene layer increases the number of dips by one.[40,41] Before Rb deposition, the surface consists mainly of monolayer graphene and the buffer layer, with the monolayer showing the characteristic reflectivity dip in the LEEM-IV spectrum around 4 eV. After Rb deposition, the LEEM-IV spectra are attenuated, but the number of dips is unchanged in both the monolayer and the buffer layer regions. Therefore, we can exclude the intercalation of Rb at the buffer layer/SiC interface. Additionally, a shift in the position of the dip by ~0.5 eV towards lower energies in the LEEM-IV spectrum is observed. As the energetic position of the graphene interlayer states strongly depends on the layer distance,[42,43] such a shift might be related to a change in the interlayer spacing of the graphene due to Rb intercalation. However, such an interpretation of the LEEM-IV spectra is difficult as it does not take into account the influence of the Rb interlayer on the electronic properties of the system, which affects the reflectivity. Nevertheless, LEEM further supports the LEED and STM conclusions that Rb is intercalated and resides between monolayer graphene and the buffer layer, without intercalating the buffer layer.

Furthermore, after Rb intercalation, the threshold energy for total reflection of electrons from the surface is shifted by approximately 2 eV to lower energies, indicating a change in the work function by the same amount. This shift is larger than the work function change of 0.5 eV calculated by DFT for Rb intercalation (see section S6 in the ESI†) and more comparable to the work function change expected for Rb adsorption. However, based on our STM results, we can rule out adsorption of Rb on monolayer graphene and instead, consistent with the STM results, attribute the observed shift to an overestimation of the work function by LEEM due to inhomogeneous intercalation: at the threshold voltage, the kinetic energy of the incoming electrons is minimal directly above the surface. This makes them susceptible to lateral electric fields emerging between regions with different work functions on the surface in close proximity to each other, resulting in an overestimation of work function changes in the electron volt range.[44] Nevertheless, the negative shift of the apparent work function still confirms substantial n-type charge transfer doping of graphene by Rb intercalation, which, from DFT results, we estimate to result in a downward shift of the Dirac point by approximately 1.1 eV.

Selected annealing steps above RT provide information about Rb diffusion and de-intercalation kinetics. As graphene samples dosed with Rb at RT are heated just above room temperature (50 °C), any sign of Rb ordering ((2 × 2) or $(\sqrt{3} \times \sqrt{3})$ R30°) disappears from the diffraction pattern. This is also confirmed by STM imaging, which reveals that Rb is still intercalated as a single layer underneath the topmost graphene surface and above the buffer layer, but without apparent order (as reported and further discussed in section S4 in the ESI†).

Analysis of the Rb-intercalated graphene area obtained from large-scale STM imaging, reported in Fig. 8 (and section S4 in the ESI†), shows the presence of two temperature regimes. At first, we observe an increase in the extent of intercalated areas. Indeed, after annealing the sample at 150 °C,

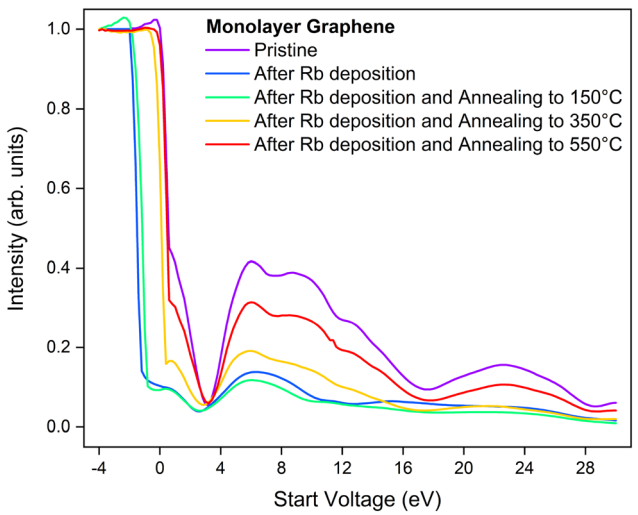

Fig. 7 LEEM-IV spectra of monolayer graphene obtained after Rb deposition at room temperature followed by annealing cycles. The spectra were extracted and averaged over regions of interest of approximate size (250 nm × 250 nm) and normalized to the intensity of the threshold energy for total reflection of electrons. The LEEM-IV spectrum of pristine monolayer graphene is included as a reference.

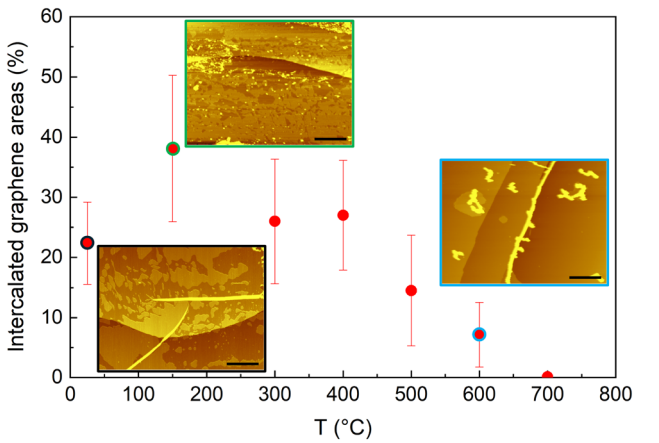

Fig. 8 Statistical analysis of several STM images (500 nm × 500 nm) reporting the fraction of the Rb-intercalated graphene area as a function of annealing temperature (*T*). Inset of the graph: STM images of size (500 nm × 380 nm) representative of the sample surface after Rb deposition at RT (black) and subsequent annealing up to 150 °C (green) and 600 °C (blue). Colors for the frames of the STM images correspond to the colors of the data points highlighted in the plot.

the intercalated area almost doubles with respect to the initial fraction (from ~20% to ~40%). This requires a supply of Rb; *i.e.*, for this to happen, there must be an Rb source in the sample. Since no adsorbed Rb atoms or clusters are observed after deposition at room temperature, Rb is likely provided by the wrinkles. Still, diffusion of the ordered intercalated Rb atoms may happen, also leading to an enlargement of the intercalated region.

At temperatures above 150 °C, desorption sets in. The fraction of the intercalated area decreases, and the single intercalated islands shrink in size and fragment. Rb clusters, not present before, start appearing on the graphene surface. Already at 300 °C, the area fraction of the intercalated islands returns to the RT value. The desorption process continues up to approximately 700 °C, when the intercalated fraction reduces to zero. The surface is left with wrinkles, a few dispersed clusters, and sparse Rb multilayered islands. This demonstrates that the intercalation process is reversible. The LEEM analysis shown in Fig. 7 reveals consistent results and confirms the reversibility of the intercalation process on a different length scale. With annealing cycles above 350 °C, the shape of LEEM-IV progressively changes towards that of pristine graphene. After annealing the sample at 550 °C, the work function and the position of the dip return to the values of pristine graphene, indicating Rb desorption and retrieval of the initial pristine surface.

4 Discussion

Changes in the diffraction pattern revealed a phase transition from a well-ordered Rb (2 × 2) structure to a more closely packed Rb $(\sqrt{3} \times \sqrt{3})$ R30° structure. Both structures, as confirmed by STM, LEED and LEEM, correspond to the formation of a well-ordered alkali-metal layer intercalated below the topmost graphene layer, *i.e.*, between the buffer layer and monolayer graphene. The phase transition is obtained by increasing the Rb coverage (as shown in the case of RT-Rb deposition) or by allowing diffusion to take place with annealing cycles (as shown in the case of LT-Rb deposition). At the same time, we observe no evidence of Rb intercalation below the buffer layer, but only disordered adsorption of Rb atoms on the surface of the buffer layer. On the other hand, on monolayer graphene, we only observe intercalation of Rb atoms and no adsorption on the monolayer surface at RT. This observation aligns with our results from DFT, which show that intercalation of Rb atoms between the buffer layer and monolayer graphene is an energetically favorable process compared to adsorption on the monolayer graphene surface. At the same time, DFT shows that adsorption of Rb atoms on the buffer layer surface is more favorable than Rb intercalation at the buffer layer/substrate interface.

The (2 × 2) structure is analogous to that of bulk C_8Rb. Previous experiments on Rb deposition onto graphite showed that Rb atoms readily intercalate the graphite surface above 80 K, forming a (2 × 2) monolayer under the topmost graphene layer before further diffusing into the bulk.[16,17,45] Additionally, experiments on epitaxial bilayer graphene grown on SiC(0001) reported that Rb atoms readily intercalate at 80 K between the two graphene layers with a (2 × 2) ordering.[9,10] However, for Rb atoms deposited on epitaxial monolayer graphene (*i.e.*, the same system investigated in this work), either at room temperature[46] or at low temperature,[9,46] no superstructure was observed previously, which is in apparent contrast to our results. However, we have indeed shown that the (2 × 2) diffraction pattern obtained by room-temperature Rb deposition is rather unstable and completely disappears within 20 min. This lack of stability may suggest why this phase was not observed in previous reports. In turn, when Rb is deposited at low temperature, the (2 × 2) diffraction pattern appears with low intensity and with a high background. In addition to the presence of an ordered Rb-intercalated structure, there is an amorphous Rb overlayer that fully covers the sample surface. This latter might have, again, hindered the visualization of ordered phases in previous reports.

The emergence of a $(\sqrt{3} \times \sqrt{3})$ R30° periodicity produced by a single intercalated Rb layer is quite unexpected and a novelty. The $(\sqrt{3} \times \sqrt{3})$ R30° structure pertains to an Rb–Rb distance of 426 pm, which corresponds to compression of the Rb lattice by ~10% compared to the nearest neighbor distance of Rb atoms in their bulk crystal structure (484 pm).[38] However, such an intralayer compression is feasible when the Rb intercalated atoms are almost completely ionized, with the electrons residing in the neighboring graphene and buffer layers.[9,11] The $(\sqrt{3} \times \sqrt{3})$ R30° structure has been frequently observed for smaller AMs (*e.g.*, Li and Na) intercalated in the C_6AM form both in graphite[16] and epitaxial monolayer graphene.[20] In the latter system, the Li- $(\sqrt{3} \times \sqrt{3})$ R30° structure forms between the graphene and the buffer layer, after the buffer layer is intercalated with Li and detached from the SiC. Recently, it has been shown that the formation of AM bilayers between two graphene sheets, corresponding to a $C_6AM_2C_6$ configuration, also leads to $(\sqrt{3} \times \sqrt{3})$ R30° periodicity.[47] However, we can exclude such a mechanism for Rb-intercalated monolayer graphene/SiC, as the resulting layer separation would be too large to be compatible with the layer separation that we measure *via* STM.

Now, based on these experimental observations, we can understand how Rb intercalation in monolayer graphene occurs. Rb has sufficient mobility on the graphene surface, even at temperatures as low as 100 K, so that it readily forms a wrinkle network. This represents the first intercalation stage of Rb under the topmost graphene layer and likely occurs at the SiC steps and graphene defects. When Rb is deposited at low temperatures, the sticking coefficient of the surface is higher than that at RT. A fraction of Rb atoms readily intercalate in extended areas and arrange with a (2 × 2) periodicity, and the remaining Rb atoms are amorphously adsorbed on the surface. Since diffusion is limited at low temperature, the structure is stable. As the sample temperature is increased towards room temperature, Rb atoms can more easily diffuse, and those in the amorphous overlayer can intercalate as well.

This leads to a change in the structural arrangement of Rb atoms in the intercalated areas, which become more densely packed and show a $(\sqrt{3} \times \sqrt{3})$ R30° ordering.

On the other hand, when Rb is evaporated at room temperature, there is a balance between adsorption and desorption of Rb atoms. All Rb atoms that stick to the surface are readily intercalated. The higher diffusion rate of Rb atoms at RT establishes a dynamic equilibrium of the intercalated atoms beneath the graphene surface. This dynamic equilibrium gives rise to a metastable (2 × 2) ordering. However, once the density of neighboring Rb atoms is high enough upon deposition of further material, intercalated Rb atoms arrange into a stable closely packed $(\sqrt{3} \times \sqrt{3})$ R30° structure.

All these processes occur between graphene and the buffer layer. The selective intercalation of Rb under monolayer graphene, rather than under the buffer layer, is caused by both kinetic and energetic reasons. Intercalation of Rb atoms below the buffer layer requires breaking of the partial covalent bonding between the buffer layer and the SiC substrate. Most metals acquire the required energy to decouple the buffer layer *via* high-temperature annealing.[48] However, deintercalation and desorption of Rb already begin at temperatures above 150 °C. This suggests that at lower temperatures, Rb atoms may not have sufficient energy to overcome the diffusion barrier required to penetrate beneath the buffer layer and decouple it from the SiC substrate. Additionally, our DFT calculations (see section S7 in the ESI†) indicate that intercalation under the buffer layer is energetically unfavorable due to the atomic size of Rb. Since the buffer layer is partially covalently bonded to the SiC substrate, intercalants must saturate the resulting dangling bonds upon decoupling. Unlike smaller species such as Li,[20] the large Rb–Rb nearest-neighbor distance prevents the effective saturation of all dangling bonds, further suppressing intercalation. As a result, Rb intercalation occurs preferentially between monolayer graphene and the buffer layer, where such constraints are absent.

5 Conclusions

We have showcased a coverage- and temperature-dependent experiment of Rb intercalation under epitaxial monolayer graphene on SiC(0001). Using LEED, STM, LEEM, and μ-LEED measurements, supported by DFT calculations, we have demonstrated that Rb atoms intercalate the topmost graphene layer, but not the buffer layer. The intercalated Rb atoms form an alkali metal interlayer, which shows two different periodicities compared to the graphene lattice, *i.e.*, a (2 × 2) and a $(\sqrt{3} \times \sqrt{3})$ R30° structure. Rb intercalation almost doubles the distance between monolayer graphene and the buffer layer, as confirmed by DFT analysis, and induces extensive doping of the graphene. By performing annealing cycles at high temperatures, we have shown that after a first stage in which diffusion prevails over desorption and the intercalated areas expand, desorption sets in, and at approximately 600 °C, we could retrieve the original surface, demonstrating the reversibility of the intercalation process.

Author contributions

L. F. – conceptualization, investigation, formal analysis, visualization, writing – original draft, and writing – review & editing; S. V. – conceptualization, investigation, validation, and writing – review & editing; T. O. M. – investigation, resources, and writing – review & editing; L. B.: investigation, formal analysis, and writing – review & editing; A. R., N. M., and C. C.: resources and writing – review & editing; J. I. F. – validation and writing – review & editing; A. L. – investigation, supervision, resources, and writing – review & editing; and S. H. – conceptualization, resources, validation, writing – review & editing, supervision, and project administration.

Data availability

The data supporting this article have been included as part of the ESI.†

Conflicts of interest

There are no conflicts to declare.

Acknowledgements

We acknowledge financial support from the PNRR MUR project PE0000023-NQSTI funded by the European Union-NextGenerationEU.

References

1 K. Fredenhagen and G. Cadenbach, *Z. Anorg. Allg. Chem.*, 1926, **158**, 249–263.
2 M. Inagaki, *J. Mater. Res.*, 1989, **4**, 1560–1568.
3 J. Xu, Y. Dou, Z. Wei, J. Ma, Y. Deng, Y. Li, H. Liu and S. Dou, *Adv. Sci.*, 2017, **4**, 1700146.
4 C. Bisio, J. Brendlé, S. Cahen, Y. Feng, S.-J. Hwang, K. Melanova, M. Nocchetti, D. O'Hare, P. Rabu and F. Leroux, *Dalton Trans.*, 2024, **53**, 14525–14550.
5 Y. Li, Y. Lu, P. Adelhelm, M.-M. Titirici and Y.-S. Hu, *Chem. Soc. Rev.*, 2019, **48**, 4655–4687.
6 M. Xue, G. Chen, H. Yang, Y. Zhu, D. Wang, J. He and T. Cao, *J. Am. Chem. Soc.*, 2012, **134**, 6536–6539.
7 J. L. McChesney, A. Bostwick, T. Ohta, T. Seyller, K. Horn, J. González and E. Rotenberg, *Phys. Rev. Lett.*, 2010, **104**, 136803.
8 M. Hell, N. Ehlen, G. Marini, Y. Falke, B. V. Senkovskiy, C. Herbig, C. Teichert, W. Jolie, T. Michely, J. Avila,

G. D. Santo, D. M. de la Torre, L. Petaccia, G. Profeta and A. Grüneis, *Nat. Commun.*, 2020, **11**, 1340.
9 J. Kleeman, K. Sugawara, T. Sato and T. Takahashi, *Phys. Rev. B: Condens. Matter Mater. Phys.*, 2013, **87**, 195401.
10 J. Kleeman, K. Sugawara, T. Sato and T. Takahashi, *J. Phys. Soc. Jpn.*, 2014, **83**, 124715.
11 T. Kaneko and R. Saito, *Surf. Sci.*, 2017, **665**, 1–9.
12 G. Csányi, P. B. Littlewood, A. H. Nevidomskyy, C. J. Pickard and B. D. Simons, *Nat. Phys.*, 2005, **1**, 42–45.
13 A. P. Durajski, K. M. Skoczylas and R. Szczęśniak, *Phys. Chem. Chem. Phys.*, 2019, **21**, 5925–5931.
14 J. Kohn, N. Rudolph, M. S. Bigelow, M. Spanjers, B. K. Stuhl, B. L. Kasch, S. E. Olson, E. A. Imhof, D. A. Hostutler and M. B. Squires, *Rev. Sci. Instrum.*, 2020, **91**, 035108.
15 B. Lu, N. Ru, J. Duan, Z. Li and J. Qu, *ACS Omega*, 2023, **8**, 21842–21852.
16 M. Caragiu and S. Finberg, *J. Phys.: Condens. Matter*, 2005, **17**, R995.
17 J. Algdal, T. Balasubramanian, M. Breitholtz, T. Kihlgren and L. Walldén, *Surf. Sci.*, 2007, **601**, 1167–1175.
18 M. Petrović, I. Šrut Rakić, S. Runte, C. Busse, J. T. Sadowski, P. Lazić, I. Pletikosić, Z.-H. Pan, M. Milun, P. Pervan, N. Atodiresei, R. Brako, D. Šokčević, T. Valla, T. Michely and M. Kralj, *Nat. Commun.*, 2013, **4**, 2772.
19 T. Huempfner, F. Otto, T. Fritz and R. Forker, *Adv. Mater. Interfaces*, 2022, **9**, 2200585.
20 S. Fiori, Y. Murata, S. Veronesi, A. Rossi, C. Coletti and S. Heun, *Phys. Rev. B*, 2017, **96**, 125429.
21 W. J. Shin, S. W. Jung, Y. Sohn, S. H. Ryu, M. Huh and K. S. Kim, *Curr. Appl. Phys.*, 2020, **20**, 484–488.
22 K. V. Emtsev, A. Bostwick, K. Horn, J. Jobst, G. L. Kellogg, L. Ley, J. L. McChesney, T. Ohta, S. A. Reshanov, J. Röhrl, E. Rotenberg, A. K. Schmid, D. Waldmann, H. B. Weber and T. Seyller, *Nat. Mater.*, 2009, **8**, 203–207.
23 A. Rossi, D. Spirito, F. Bianco, S. Forti, F. Fabbri, H. Büch, A. Tredicucci, R. Krahne and C. Coletti, *Nanoscale*, 2018, **10**, 4332–4338.
24 D. Nečas and P. Klapetek, *Cent. Eur. J. Phys.*, 2012, **10**, 181–188.
25 A. Locatelli, L. Aballe, T. O. Mentes, M. Kiskinova and E. Bauer, *Surf. Interface Anal.*, 2006, **38**, 1554–1557.
26 T. O. Menteş, G. Zamborlini, A. Sala and A. Locatelli, *Beilstein J. Nanotechnol.*, 2014, **5**, 1873–1886.
27 J. J. Mortensen, A. H. Larsen, M. Kuisma, A. V. Ivanov, A. Taghizadeh, A. Peterson, A. Haldar, A. O. Dohn, C. Schäfer, E. Ö. Jónsson, E. D. Hermes, F. A. Nilsson, G. Kastlunger, G. Levi, H. Jónsson, H. Häkkinen, J. Fojt, J. Kangsabanik, J. Sødequist, J. Lehtomäki, J. Heske, J. Enkovaara, K. T. Winther, M. Dulak, M. M. Melander, M. Ovesen, M. Louhivuori, M. Walter, M. Gjerding, O. Lopez-Acevedo, P. Erhart, R. Warmbier, R. Würdemann, S. Kaappa, S. Latini, T. M. Boland, T. Bligaard, T. Skovhus, T. Susi, T. Maxson, T. Rossi, X. Chen, Y. L. A. Schmerwitz, J. Schiøtz, T. Olsen, K. W. Jacobsen and K. S. Thygesen, *J. Chem. Phys.*, 2024, **160**, 092503.
28 J. P. Perdew, K. Burke and M. Ernzerhof, *Phys. Rev. Lett.*, 1996, **77**, 3865–3868.
29 E. Caldeweyher, C. Bannwarth and S. Grimme, *J. Chem. Phys.*, 2017, **147**, 034112.
30 E. Caldeweyher, S. Ehlert, A. Hansen, H. Neugebauer, S. Spicher, C. Bannwarth and S. Grimme, *J. Chem. Phys.*, 2019, **150**, 154122.
31 E. Caldeweyher, J.-M. Mewes, S. Ehlert and S. Grimme, *Phys. Chem. Chem. Phys.*, 2020, **22**, 8499–8512.
32 C. Riedl, C. Coletti and U. Starke, *J. Phys. D: Appl. Phys.*, 2010, **43**, 374009.
33 A. T. N'Diaye, R. van Gastel, A. J. Martínez-Galera, J. Coraux, H. Hattab, D. Wall, F.-J. Meyer zu Heringdorf, M. Horn von Hoegen, J. M. Gómez-Rodríguez, B. Poelsema, C. Busse and T. Michely, *New J. Phys.*, 2009, **11**, 113056.
34 P. Sutter, J. T. Sadowski and E. Sutter, *Phys. Rev. B: Condens. Matter Mater. Phys.*, 2009, **80**, 245411.
35 L. Bußß, N. Braud, M. Ewert, M. Jugovac, T. O. Menteş, A. Locatelli, J. Falta and J. I. Flege, *Ultramicroscopy*, 2023, **250**, 113749.
36 L. Bußß, G. Zamborlini, C. Sulaiman, M. Ewert, M. Cinchetti, J. Falta and J. I. Flege, *Carbon*, 2025, **231**, 119600.
37 D. Lide, *CRC Handbook of Chemistry and Physics*, Taylor & Francis, 85th edn, 2004, vol. 85.
38 G. Grosso and G. P. Parravicini, *Solid State Physics*, Elsevier Science, 2013.
39 H. Hibino, H. Kageshima, F. Maeda, M. Nagase, Y. Kobayashi and H. Yamaguchi, *Phys. Rev. B: Condens. Matter Mater. Phys.*, 2008, **77**, 075413.
40 P. Sutter, P. Albrecht, X. Tong and E. Sutter, *J. Phys. Chem. C*, 2013, **117**, 6320–6324.
41 C. Coletti, K. V. Emtsev, A. A. Zakharov, T. Ouisse, D. Chaussende and U. Starke, *Appl. Phys. Lett.*, 2011, **99**, 081904.
42 R. M. Feenstra, N. Srivastava, Q. Gao, M. Widom, B. Diaconescu, T. Ohta, G. L. Kellogg, J. T. Robinson and I. V. Vlassiouk, *Phys. Rev. B: Condens. Matter Mater. Phys.*, 2013, **87**, 041406.
43 N. Srivastava, Q. Gao, M. Widom, R. M. Feenstra, S. Nie, K. F. McCarty and I. V. Vlassiouk, *Phys. Rev. B: Condens. Matter Mater. Phys.*, 2013, **87**, 245414.
44 J. Jobst, L. M. Boers, C. Yin, J. Aarts, R. M. Tromp and S. J. Van Der Molen, *Ultramicroscopy*, 2019, **200**, 43–49.
45 D. Igarashi, R. Tatara, R. Fujimoto, T. Hosaka and S. Komaba, *Chem. Sci.*, 2023, **14**, 11056–11066.
46 S. Watcharinyanon, C. Virojanadara and L. Johansson, *Surf. Sci.*, 2011, **605**, 1918–1922.
47 Y.-C. Lin, R. Matsumoto, Q. Liu, P. Solís-Fernández, M.-D. Siao, P.-W. Chiu, H. Ago and K. Suenaga, *Nat. Commun.*, 2024, **15**, 425.
48 N. Briggs, Z. M. Gebeyehu, A. Vera, T. Zhao, K. Wang, A. De La Fuente Duran, B. Bersch, T. Bowen, K. L. Knappenberger and J. A. Robinson, *Nanoscale*, 2019, **11**, 15440–15447.

